Seismogenic structure along the deformation front off SW Taiwan revealed by the aftershocks of the 2017 Tainan near-shore earthquake with ocean bottom seismometers

Wen-Nan Wu [a], Chung-Liang Lo [b], Wen-Bin Doo [c], Jing-Yi Lin [b,c], Shu-Kun Hsu [b,*]

[a] College of Oceanography, Hohai University, No. 1, Xikang Road, Gulou Dist., Nanjing, Jiangsu 210098, China
[b] Department of Earth Sciences, National Central University, No. 300, Zhongda Road, Zhongli District, Taoyuan City 32001, Taiwan
[c] Center for Environmental Studies, National Central University, No. 300, Zhongda Road, Zhongli Dist., Taoyuan City 32001, Taiwan

ABSTRACT

Located in the northern end of the Manila Trench, the deformation front (DF) off southwestern Taiwan is considered as a potential area for generating hazardous earthquakes and tsunamis. However, this area has been relatively seismically quiet, and the seismogenic structure has been unclear, particularly in the middle-to-lower crust. On February 10, 2017, an M_w5.3 earthquake occurred in the near-shore area of Tainan in SW Taiwan, which provides us with a good opportunity to study the seismogenic structure of this area. Five ocean bottom seismometers (OBSs) were deployed to cover the mainshock source area from February 13 to March 1, 2017, to record the aftershock data. All the OBSs were successfully recovered and, the P- and S-wave arrival were manually identified. In collaboration with arrival times from the Central Weather Bureau of Taiwan, we simultaneously determined the 1-D optimal Vp and Vs velocity models and hypocenter locations. The inversion results show that the upper crust (<15 km) has a relatively low velocity, and most events are confined between 10 and 15 km depth. The relocated epicenters were all in areas with positive gravity anomalies, and most of them formed a NE-SW striking seismogenic structure that was approximately parallel to the surface trace of the DF and did not link to any known active faults in SW Taiwan. The hypocenters illustrate a conjugate fault system comprising of a SW-dipping NE-SW striking fault and an SE-dipping NW-SE striking fault. Based on focal mechanisms and aftershock distribution, we demonstrate that the 2017 Tainan near-shore earthquake may result from the reactivation of pre-existing faults, and the driving force comes from the bending stresses of the subducting Eurasia Plate at the Manila Trench. Given the active subduction processes offshore of Taiwan, such slab-flexural-related earthquakes must be considered in seismic and tsunami hazard assessments.

1. Introduction

The island of Taiwan is in the active collision zone between the Eurasia Plate and the Philippine Sea Plate, where the Philippine Sea Plate is northwestward converging at a high rate of approximately 8 cm/yr relative to the Eurasia Plate (Tsai et al., 2015; Yu et al., 1997) (Fig. 1). In the north, the Philippine Sea Plate subducts beneath the Eurasia Plate along the Ryukyu Trench, while to the south, the Eurasia Plate subducts beneath the Philippine Sea Plate along the Manila Trench. This active tectonic context generated numerous earthquakes.

As shown in Fig. 1, in addition to large earthquakes related to the subduction, nearly half of the devastating earthquakes occurred in the middle and southwestern portions of Taiwan due to the ongoing collision between the Philippine Sea Plate and the Eurasia Plate. In particular, the deformation front (DF), the frontal limit of the fold-and-thrust belt of the Taiwan orogen (Liu et al., 1997; Yang et al., 2016), generates several moderate-to-large disastrous earthquakes. For example, the devastating 1906 Ms7.1 Meishan earthquake, 1935 Ms7.2 Hsinchu-Taichung earthquake, 1941 Ms7.2 Cungpu earthquake, 1964 Ms7.0 Tainan-Chiayi earthquake and 1999 Mw7.3 Chi-Chi earthquake occurred near the DF and caused surface ruptures, huge damage, and death (Kao and Chen, 2000; Wang, 1998).

The DF in SW Taiwan is widely assumed to extend offshore and connects to the northward elongation of the Manila Trench, which is the northernmost portion of the South China Sea (e.g., Lin et al., 2008; Liu et al., 1997). However, the details of the transition from the Manila

Trench to the DF are still unclear (e.g., Han et al., 2017; Yu, 2004). Most importantly, by analogy with the occurrence of the hazardous earthquakes that occurred near the inland DF, the thrust front of the DF off SW Taiwan may also possess the potential to generate large earthquakes. Several ENE-WSW-trending normal faults have been identified off SW Taiwan (Huang et al., 2004; Liu et al., 2004; Liu et al., 1997; Yang et al., 2016), which may cause submarine landslides and tsunamis. Therefore, we believe that the areas off SW Taiwan, especially near the DF, have a high potential for generating hazardous earthquakes and tsunamis and should be considered in geo-hazard mitigation efforts for the Taiwan region.

Many factors affect fault system ruptures and earthquake magnitudes (e.g., Aochi et al., 2000; Bai and Ampuero, 2017). Nevertheless, an earthquake magnitude can be estimated from the fault geometry (i.e., the fault length and width) (e.g., Shyu et al., 2005; Shyu et al., 2020; Wells and Coppersmith, 1994; Wu et al., 2017). It is thus critical to

delineate the seismogenic structure off SW Taiwan in detail to improve the accuracy of scenarios developed for future disastrous earthquakes in this area. Several seismic experiments in SW Taiwan have been conducted to explore subsurface structures (e.g., Han et al., 2017; Lester et al., 2012; Lester et al., 2014; Liu et al., 2004; Liu et al., 1997; Yu, 2004). However, for these seismic experiments, the most reliable portion in depth was limited to the upper crust (<15 km) because the seismic source energy was too weak or largely attenuated or both. It is noticeable that the area off SW Taiwan is relatively seismically quiet (Fig. 2a), and the spatial distribution of current permanent inland seismic stations is not suitable for seismological studies (e.g., earthquake source parameters and seismic travel time tomographic studies) for this area. Hence, seismic tomographic images from recent studies are featureless and the seismogenic structure in this area remains ambiguous, particularly with respect to the depth from the middle crust to the upper mantle.
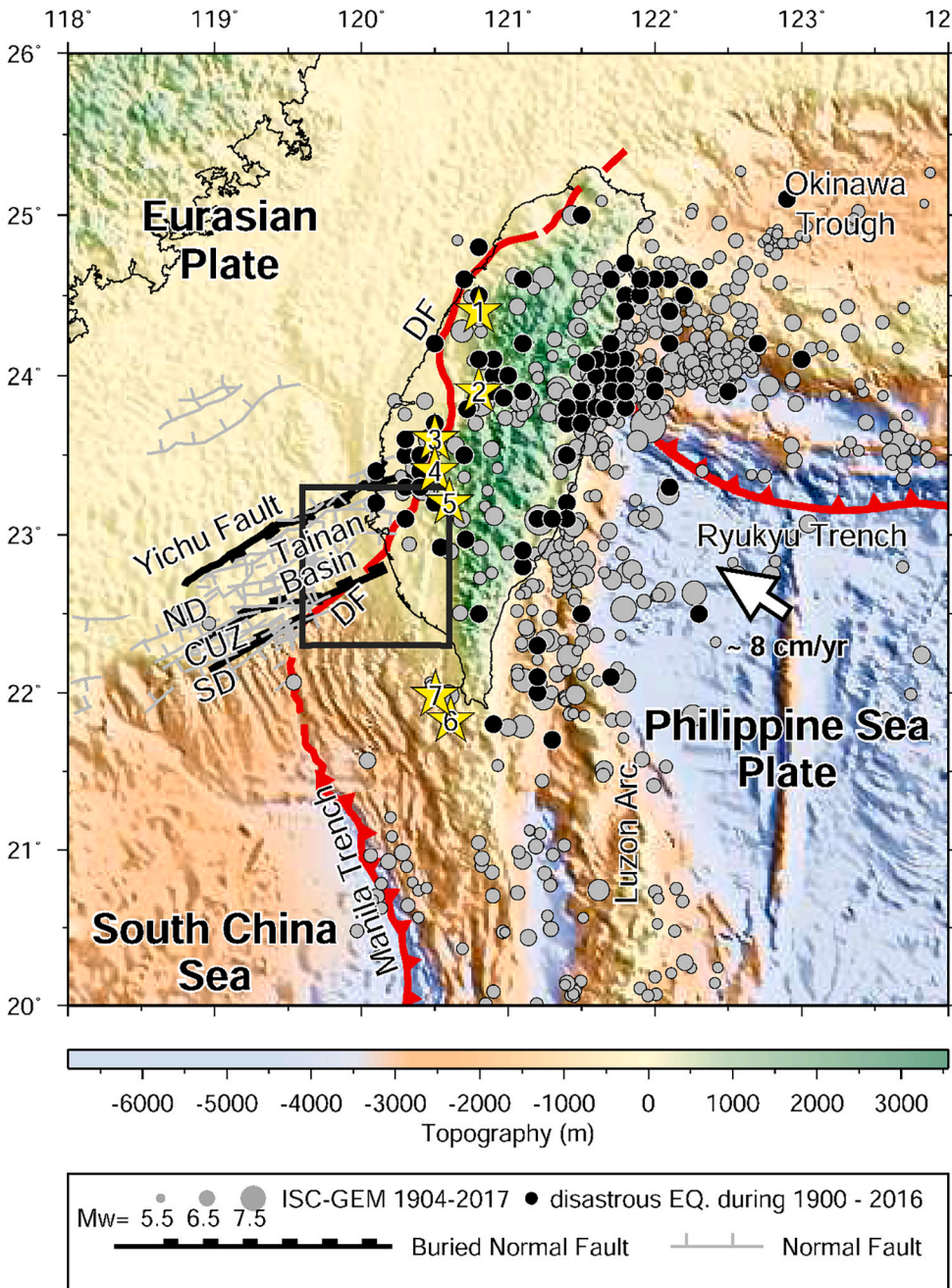

Fig. 1. Tectonic framework of the Taiwan orogen. Topography/bathymetry data of the region was taken from the version 20.1 of global marine bathymetry database (Sandwell and Smith, 1997). The open arrow shows the plate motion direction of the Philippine Sea Plate relative to the Eurasia Plate (Tsai et al., 2015; Yu et al., 1997). The box shows our study area. Most portion of the study area is in the Tainan Basin, which consists of the northern depression (ND), central uplift zone (CUZ), and southern depression (SD) (Lester et al., 2012; Liao et al., 2016). Surface traces of normal faults are compiled from Liu et al. (1997), Liu et al. (2004), Huang et al. (2004), and Yang et al. (2016). Gray circles are intermediate-large earthquakes from the ISC–GEM catalog (Storchak et al., 2013) between 1904 and 2017. Black circles are disastrous earthquakes between 1900 and 2016 reported by the Central Weather Bureau (CWB) of Taiwan (https://scweb.cwb.gov.tw/zh-tw/page/disaster). Solid stars represent the disastrous earthquakes that occurred near the deformation front (DF) and was mentioned in the context. 1: 1935 Ms7.2 Hsinchu-Taichung earthquake; 2: 1999 Mw7.3 Chi-Chi earthquake; 3: 1906 Ms7.2 Meishan earthquake; 4: Ms7.2 Cungpu earthquake; 5: 1964 Ms7.0 Tainan-Chiayi earthquake; 6: the first event of the 2006 Mw7.0 Pingtung earthquake doublet; 7: the second event of the 2006 Mw6.9 Pingtung earthquake doublet.
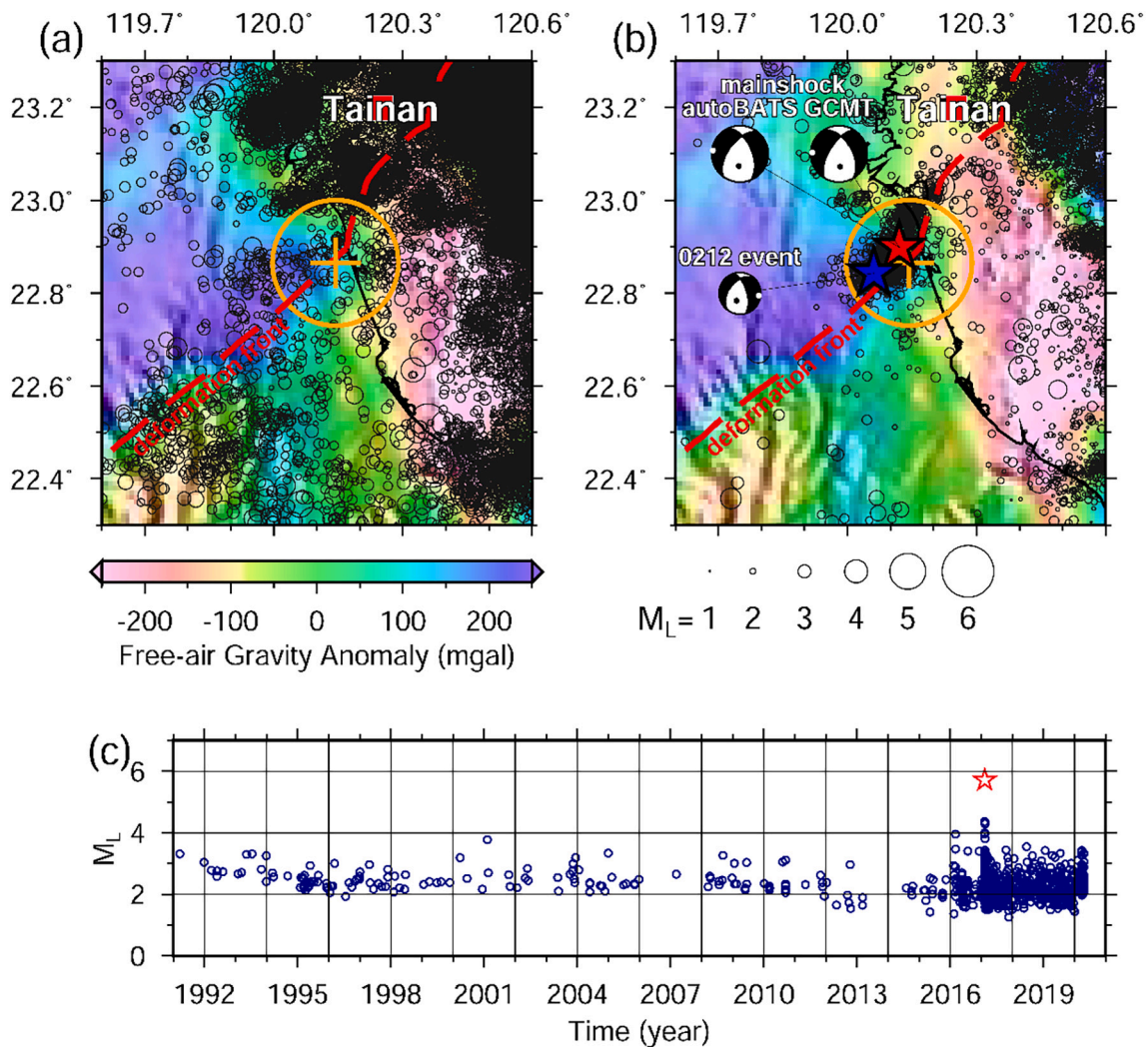
Fig. 2. Spatial distribution of seismicity before and after the Tainan earthquake, is shown in (a) and (b), respectively. The background is colored with the free air gravity anomaly from the global database of Sandwell et al. (2014). Seismicity data comes from the CWB catalog between January 1991 and April 2020. The orange cross is the revised epicenter of the Tainan earthquake reported by the CWB. The orange circle represents the range of 15 km from the mainshock epicenter, which is defined as the source area. Two solid stars are the epicenters of the mainshock and an aftershock occurred on 12 February (0212 event) from the fast earthquake report of the CWB, which were used later by the Broadband Array for Taiwan Seismology (BATS) for the moment tensor inversion (AutoBATS moment tensor catalog). Beach balls show the best double-couple solution of AutoBATS and global centroid moment tensor (GCMT) in a lower-hemisphere projection, and small solid circle and open circle represent the P- and T-axis of the focal mechanism solution, respectively. (c) Plots of earthquake magnitudes with time in the source area. An open star indicates the occurrence time and magnitude of the mainshock, showing that the Tainan earthquake is the largest event in the source area during the past three decades.

On February 10, 2017, a moderate (M_w5.3) earthquake occurred near the shore of Tainan city in SW Taiwan, hereinafter referred to as the Tainan earthquake. The quick earthquake report of the Central Weather Bureau (CWB) of Taiwan indicated that the epicenter of the mainshock is located at the surface trace of the DF (Fig. 2b). Moreover, based on the seismicity catalog operated by the CWB from January 1991 to June 2017, seismic activity in the source area (epicentral distance < of 15 km) showed that the Tainan earthquake occurred in an area with low seismic activity and is the largest event since 1991 (Fig. 2). This earthquake sequence is expected to provide critical constraints on the local seismogenic structure in this area.

The revised centroid moment tensor solutions reported by the AutoBATS (full-scanning approach on Broadband Array in Taiwan for Seismology) (Jian et al., 2018) further indicated that the focal mechanism of the mainshock with the centroid depth of 10 ± 7 km exhibits mainly normal faulting with a minor strike-slip component, which was consistent with the global centroid moment tensor solution (Dziewonski et al., 1981) with a centroid depth of 12 km (Fig. 2b). Meanwhile, an

M_w3.8 aftershock occurred on February 12 (hereinafter referred to as the 0212 event) and its focal mechanism with the centroid depth of 21 ± 5 km is consistent with that of the mainshock (Fig. 2b). It is noteworthy that one of the strikes of the AutoBATS' fault plane solution is 217°N and 219°N for the mainshock and 0212 event, respectively, which is remarkably consistent with the trend of the surface trace of the DF (Fig. 2b).

After the occurrence of the mainshock, we deployed five ocean-bottom seismometers (OBSs) to well cover the earthquake rupture area to record approximately two weeks of continuous seismic waveforms of aftershocks (Fig. 3a). By combining the arrival times of the P- and S-waves of the aftershocks from our OBS data with those from the CWB inland stations, we can increase the station coverage to improve the inversion accuracy of velocity models and aftershock locations (Fig. 3b). In this study, we take the opportunity of newly occurring events, the aftershocks of the Tainan earthquake, to shed light on the seismogenic structure near the DF offshore SW Taiwan to provide new constraints on seismogenic mechanisms and seismic hazard assessment
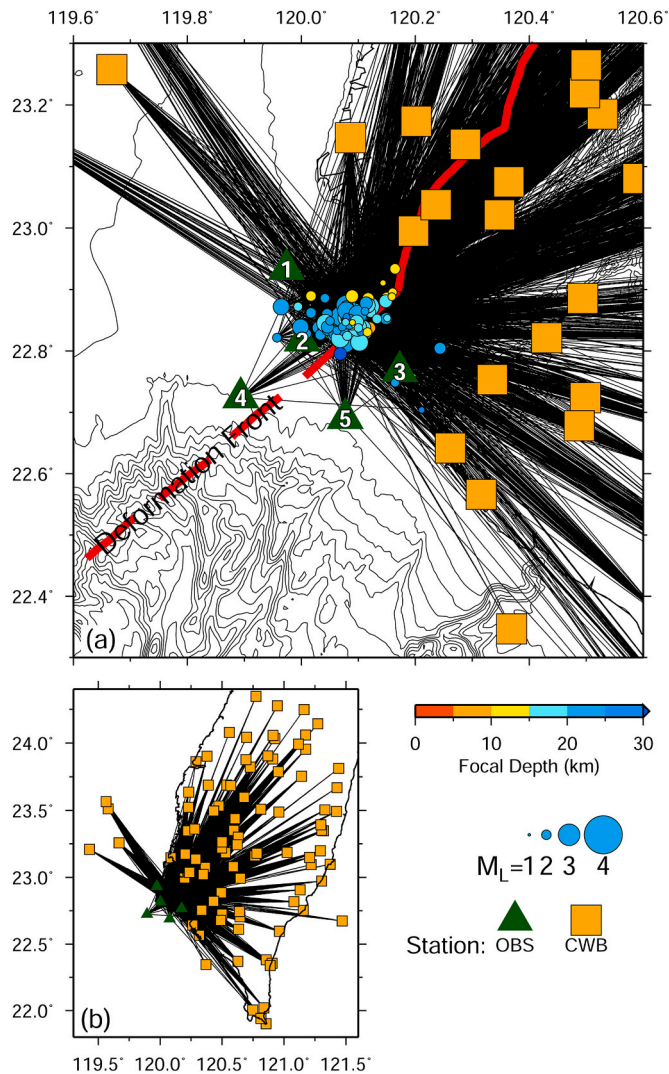
Fig. 3. (a) Bathymetric map and distribution of the ocean-bottom seismometers (green triangles), some CWB stations (brown squares), and aftershocks (solid circles) that were used for inversion. Bathymetric contours are at intervals of 100 m. Black lines are raypaths. (b) Raypaths between used stations and events are shown with black lines. (For interpretation of the references to colour in this figure legend, the reader is referred to the web version of this article.)

of the region.

2. Data and methods

2.1. Travel time data

The OBS used to record the seismic waveforms is MicrOBS Plus, which is a short-period device developed by the French Research Institute for Exploitation of the Sea (Ifremer). All OBSs are equipped with three-component 4.5 Hz geophones and one broadband-type hydrophone (Auffret et al., 2004). A total of five OBSs were deployed in the source area (Fig. 3a), and later all successfully were recovered, which provided continuous three-component waveform records from February 13 to March 1, 2017.

To obtain initial hypocenter locations and P- and S-wave arrivals recorded by both the OBS and CWB stations for further analysis, we first selected the events that had at least four P-wave first arrivals either with or without S-wave picks in our study area from the CWB earthquake bulletin during the OBS deployment period. Then, we retrieved the reliable P- and S-wave arrivals on the OBS data by manually identifying

the onset times of the P- and S-waves. As a result, we identified 85 events in which each event had at least one P- or S-wave first arrival from the OBSs. Meanwhile, CWB stations beyond 200 km are not used in the following analysis for a better approximation of a flat Earth used in the travel time determination using the 1-D ray-tracing algorithm (Kissling et al., 1994; Lin, 2013) (Fig. 3b). In addition, the better quality (weight ≤ 3.0, assigned in the CWB bulletin) in the CWB picking arrival is selected to avoid the effect of the poor-quality data on the inversion results. Finally, the total numbers of P- and S-wave arrivals from 85 earthquakes in this study were 2440 and 2306, respectively.

2.2. Inversion for the 1-D Vp and Vs models and hypocenters

To enhance the accuracy of hypocenter locations and local velocity models, we used the VELEST program proposed by Kissling et al. (1994) by simultaneously determining the P- and S-wave 1-D velocity models and the hypocenter parameters, including station corrections with minimum root mean square (RMS) of the travel time residual. Station corrections (i.e., station delay times) represent derivations from the 1-D velocity model because of the 3-D structure with respect to a reference station (Rezaeifar and Kissling, 2018). Note that the original VELST algorithm made all stations be within the top layer of the velocity model, which may introduce bias into the inversion results (Hicks et al., 2014; Kissling et al., 1994; Lin, 2013). Here, we use a revised VELST software that modifies the 1-D ray-tracing code to trace raypaths from sources to receivers; that is, we can take station elevations within different velocity layers into account for the travel time computation (Lin, 2013). The modification in the travel time prediction improves the performance of the VELEST software, which will be demonstrated in detail later in this section.

We realize that the initial velocity model affects the inversion results of the velocity models and hypocenter locations (Hicks et al., 2014; Lange et al., 2012; Wang et al., 2019). To mitigate the initial model dependency in the inversion of velocity and hypocenter, we used three different 1-D velocity models to independently generate 2000 initial velocity models by randomly perturbing ±5% each layer of the 1-D P- and S-wave reference velocity models and repeating the inversion steps. The velocity model with the minimum travel time residual was selected for the following analysis. Specifically, in addition to the CWB 1-D P- and S-wave reference velocity models of Chen and Shin (1998) (Fig. S1), we also used the 3-D velocity models of Kuo-Chen et al. (2012) and Huang et al. (2014) to determine the 1-D P- and S-wave reference velocity models by averaging over all velocity values along the raypaths from sources to receivers for each layer. The 1D velocity model derived from Kuo-Chen et al. (2012) and Huang et al. (2014) is referred to as the Kuo-Chen 1-D reference model and Hunag 1-D reference model, respectively (Fig. 4 and Fig. S2). It is noticeable that in the P- and S-wave models of the Huang et al. (2014), a thin layer of velocity structure is introduced in the shallowest 0–300 m depth, which is constrained by the borehole logging data and helpful for obtaining a more reliable near-surface velocity structure.

Before discussing the effect of the 1-D reference model on the inversion result, we first evaluate the performance of our modified 1-D ray tracing code and station delay time inversion. To this end, we performed the VELEST inversion by using the original 1-D ray tracing code and our revised version with the CWB 1-D reference model and the same control parameters without the station delay inversion. The minimum RMS of the travel time residuals is 0.917 ± 0.027 and 0.767 ± 0.034 s according to the original 1-D ray tracing code and our revised version, respectively. The significant reduction (16%) in the RMS value demonstrates that the modified 1-D ray-tracing code can effectively improve the accuracy of the travel time prediction and decrease the potential bias in the inversion result. We further found that the minimum RMS of travel time residuals decreases from 0.767 ± 0.034 to 0.663 ± 0.022 s by using the station delay inversion in the VELEST software, which indicates that the station correction can effectively reduce the effect of the
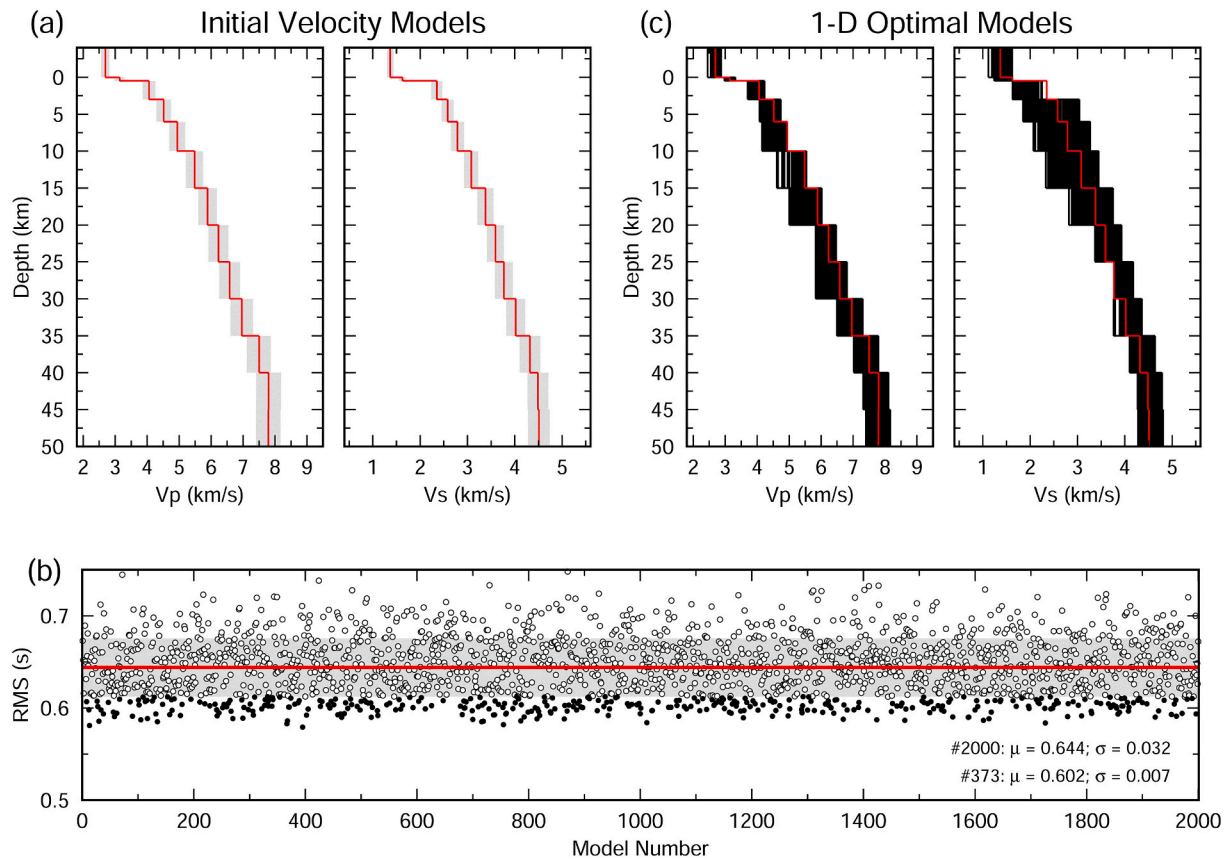
Fig. 4. (a) Initial 2000 bootstrap resamples (gray lines) of 1-D P- (left panel) and S-wave (right panel) velocity models used for inversion, which derived from ±5% within the Huang 1-D P- and S-wave reference velocity models. (b) A plot of the room-mean square (RMS) travel time residuals with initial velocity models. The red solid line indicates the mean RMS value (0.644 s), and the gray band shows the confidential area within the one standard derivation (0.032 s). Black solid circles are the optimal velocity models (373 models). The mean RMS value with one standard derivation of the 373 inversion results is 0.602 ± 0.007 s. (c) Black lines are the inverted P- (left panel) and S-wave (right panel) for the optimal velocity models. Red lines in (a) and (c) represent the P- (left panel) and S-wave (right panel) of the Huang 1-D reference velocity models. (For interpretation of the references to colour in this figure legend, the reader is referred to the web version of this article.)

lateral variation in the shallow subsurface.

Based on the above experimental results, we independently applied the VELEST program with our modified 1-D ray tracing code and the station delay inversion to the 2000 initial random Vp and Vs velocity models of CWB, Kuo-Chen and Huang 1-D reference velocity models. The inversion results show that the minimum mean RMS values with one standard derivation are 0.663 ± 0.022, 0.660 ± 0.020, and 0.644 ± 0.032 s for the CWB, Kuo-Chen and Huang 1-D reference velocity models, respectively (Fig. 4 and Fig. S1-S2). Because of the smallest mean RMS value, we used the VELEST result with the Huang 1-D reference velocity model for the following analysis.

From the 2000 inversion results of the P- and S-wave velocity models and hypocenters, the travel time residual (RMS) drops from the initial 1.137–1.420 s to the final 0.579–0.748 s after nine iterations (Fig. 4b). Note that a set of inversion results has the same RMS values because of the trade-off between the velocity models and hypocenters. Thus, rather than presenting only one inversion result with a global minimum RMS value, we prefer to present an average result from a family of inversion results with relatively low RMS residuals. The mean RMS value (0.644) minus one standard deviation (0.032) was used to determine the inversion result (0.612 s), resulting in 373 sets of the optimal inverted velocity models (Fig. 4c) and hypocenters (Fig. 5). From these 373 models, the mean RMS value with one standard derivation was 0.602 ± 0.007 s. For each event, we further determined the average hypocenter location from the 373 inversion results and computed the mean values of horizontal and vertical distance differences between the average location and the corresponding inverted hypocenters (Fig. 5). On average,

the location difference is 0.26 ± 0.08 and 0.85 ± 0.24 km in the horizontal and vertical direction, respectively, from 85 events.

The other outcome of the inversion using the VELEST software is P- and S-wave station delays, which reflect the integral effects of the 3D subsurface and deep crustal structure (Diehl et al., 2009; Rezaeifar and Kissling, 2018). The mean values of P- and S-wave station delays were obtained by averaging 373 sets of VELEST inversion results. We define the station TPUB as the reference station and set the station delays as zero, and then calculate the station delays with respect to the reference station for each station. Negative and positive station delays indicate higher velocities and lower velocities, respectively (Diehl et al., 2009; Rezaeifar and Kissling, 2018). The statistics of the P- and S-wave station delays and the spatial variation of the station delays are displayed in Fig. S3.

2.3. Relative hypocenter relocation

Earthquake relative locations have helped to delineate fault structures for seismogenic structural interpretation (e.g., Lin and Okubo, 2020; Roth et al., 2020; Shelly, 2020). Thus, we apply the shrinking box source-specific station term (SSST) method (Lin, 2018; Lin and Shearer, 2005) to improve the earthquake relative location for better delineating the seismogenic structure. The advantages of the shrinking-box SSST are that the required number of input parameters is relatively low and it can improve the absolute location accuracy (Lin and Shearer, 2005). The procedure of the shrinking-box SSST relocation algorithm involves three steps: (1) using the grid-search approach to relocate earthquakes, and
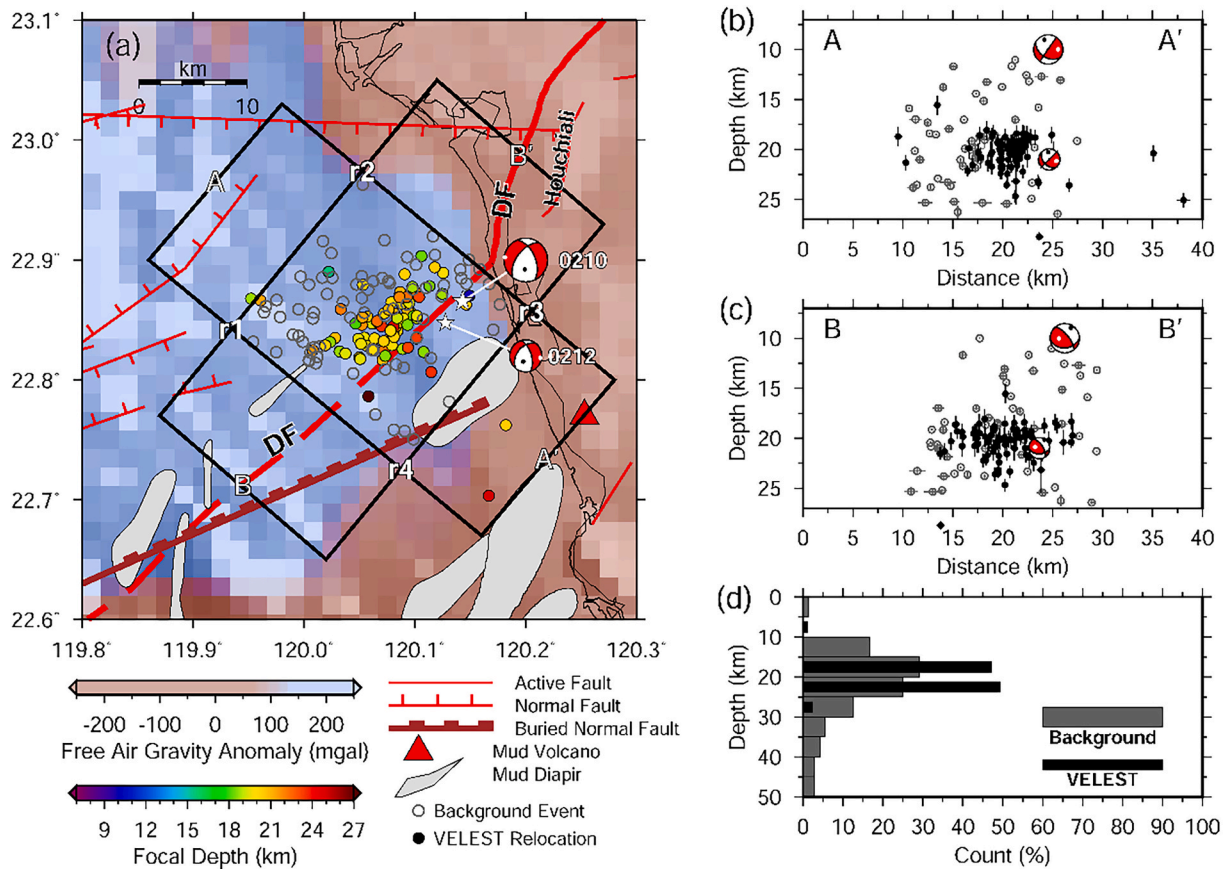
Fig. 5. (a) Distribution of the relocated aftershocks (the solid circles) by the VELEST software. The background is colored with the free air gravity anomaly from the global database of Sandwell et al. (2014). The gray open circles in the square area (defined by r1, r2, r3, and r4) are the well-constrained background seismicity (Wu et al., 2017; Wu et al., 2008). Beach balls show the best double-couple solution from the AutoBATS catalog in a lower-hemisphere projection for the 0210 event (mainshock) and the 0214 event (aftershock), respectively. The location of the two cross-sections is shown in (a). The A-A' cross-section oriented perpendicular to the strike of the DF is in (b), and the B-B' cross-section oriented parallel to the strike of the DF is in (c). Depth distribution of the relocated aftershocks along the cross-section, which including events within 10 km on each side of the profile. In (b) and (c), vertical and horizontal bar is the location uncertainty in the vertical and horizontal direction, respectively. Beach balls show the best double-couple solution in a back-hemisphere projection, and small solid circle and open circle represents the P- and T-axis of the focal mechanism solution, respectively. (d) Histogram showing the frequency versus focal depth with 5-km bin widths. Histograms comparing focal depths of earthquakes from our results (black) and background seismicity (gray).

(2) the static station term is determined by calculating the station term for each station as the mean of the residuals at that station from all events. The static station term is added to the observations for the grid-search relocation in Step 1. This process is repeated several times (Iter1). (3) The SSST is calculated for each source-receiver pair at a given station using the residuals from nearby events, which are determined by the decrease in the cutoff distance with iterations. We predefine the nearby event number (Nmax and Nmin of the first and final iteration, respectively), a sphere of the specified radius (i.e., cutoff distance, Rmax and Rmin of the first iteration and final iteration, respectively). The SSST was added to the observations for the grid-search relocation in Step 1. This process was repeated several times (Iter2). The three sequential steps form the core of the standard shrinking-box SSST method and are repeated and then stop iterating when the number of iterations exceeds a predefined maximum (Itermax).

In practice, a group of 373 velocity models, hypocenters, and station delays from the VELEST inversion results were used for the shrinking-box SSST relocation. Meanwhile, to ensure that the shrinking-box SSST has proper performance, we examined the effect of the control parameters of the shrinking-box SSST method on the earthquake relocation. For this, we performed a set of tests by changing the value of each parameter based on the spatial distribution characteristics of our data. From the RMS comparisons for different experimental results (Table S1), we found that the control parameters of the shrinking-box SSST method,

Iter1 = 3, Iter2 = 5, Nmax = 40, Nmin = 5, Rmax = 100, Rmin = 10, and Itermax = 5, can reduce the RMS value from 0.602 ± 0.007 s for the VELEST result to 0.339 ± 0.003 s, which is a reduction of approximately 44%. The distribution of the RMS of the travel time residuals for each event is shown in Fig. S4.

Finally, for each event, the final hypocenter relative location was determined by averaging the 373 sets of relocation results and then used to calculate the mean location distance difference with respect to the corresponding hypocenters. On average, the location difference is 0.44 ± 0.32 and 1.27 ± 0.32 km in the horizontal and vertical directions, respectively, from 85 events (Fig. 6).

2.4. Principal component analysis

We further quantified the first-order geometrical properties of the aftershock relative location by using a principal component analysis (e. g., Michelini and Bolt, 1986; Shearer et al., 2003). In practice, we first computed the spatial covariance matrices of the event locations regarding their means, and then determined the average values of the eigenvalues (λ_1, λ_2, λ_3, and $\lambda_1 \geq \lambda_2 \geq \lambda_3$). Finally, the corresponding eigenvectors with one standard derivation uncertainty were determined based on 1000 bootstrap resamplings of the event locations. The eigenvector with the largest eigenvalue was used to define the longest axis of an ellipsoid that describes the hypocenter distribution, whereas
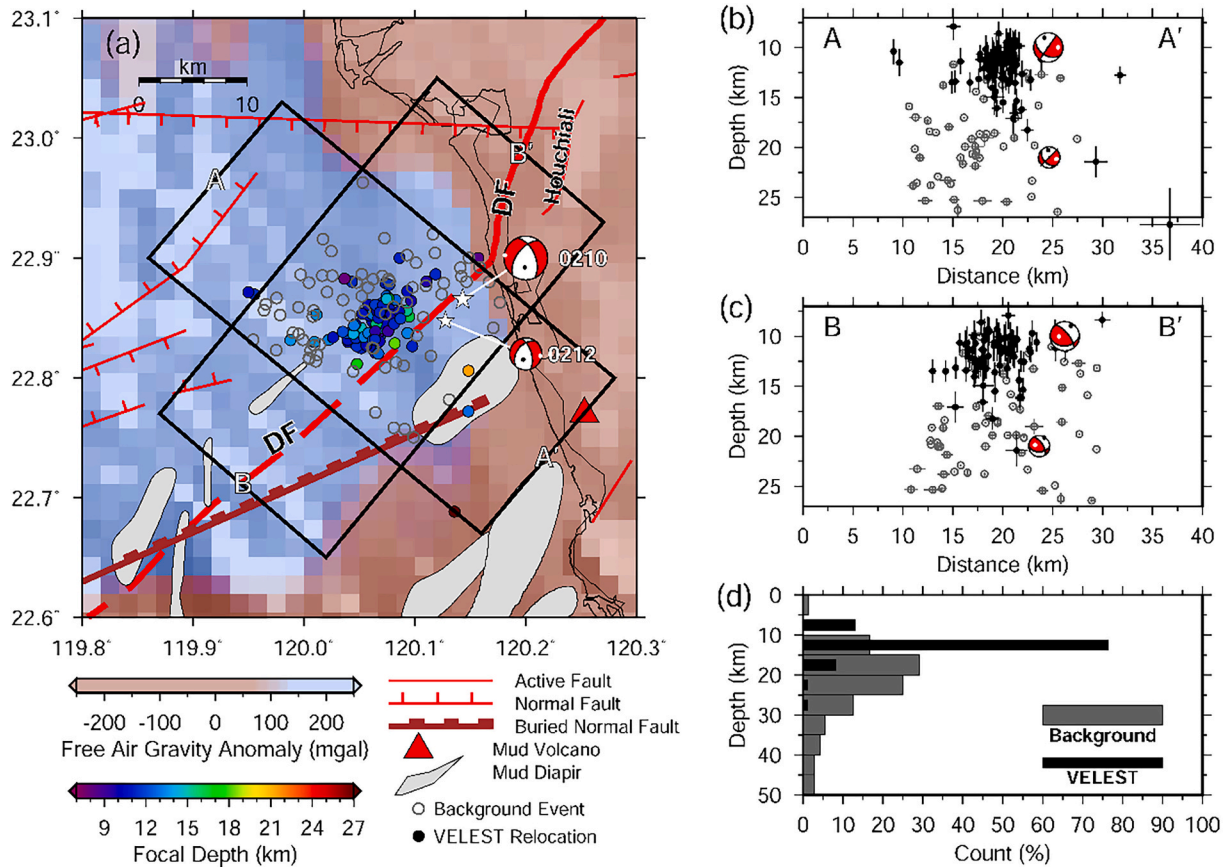
Fig. 6. Distribution of the relocated aftershocks by the shrinking-box Source-Specific Station Terms (SSST) algorithm. Layout and symbols are the same as that in Fig. 5, except that the aftershocks are relocated by the shrinking-box SSST algorithm.

the eigenvector with the smallest eigenvalue was used to define the shortest axis of the ellipsoid. To facilitate the discussion, the eigenvector with the intermediate eigenvalue was defined as the intermediate axis. We also computed the quantity $1-2\lambda_3/(\lambda_1 + \lambda_2)$, which was used to measure the degree of planarity formed by hypocenter distribution (Pang et al., 2018). The planarity of one presented a well-defined planar alignment, and a planarity of zero indicates a sphere.

2.5. Neighboring event detection

In addition to the hypocenter distribution, we detected additional events to reveal the aftershock productivity (i.e., the number of earthquakes that occurred during the OBS deployment period) around the mainshock rupture area. To this end, we used the OBS data for analysis because the OBS stations are distributed around the aftershock zone and are expected to record seismic signals of small events associated with the mainshock.

Here, we use the sliding-window cross-correlation detection method proposed by Yang et al. (2009), which is a variant of the conventional matched-filter technique (e.g., Gibbons and Ringdal, 2006; Peng and Zhao, 2009; Shelly et al., 2007). Rather than separately computing cross-correlation coefficients for three-component waveforms, the sliding-window cross-correlation simultaneously cross-correlates three-component waveforms of template events with continuous waveforms to obtain normalized cross-correlation coefficients with the recorded time. In other words, the sliding-window cross-correlation puts all seismic phase information from the three-component waveforms into one normalized cross-correction coefficient. Compared to the conventional matched-filter detection method, the sliding-window cross-correlation may not only decrease computational costs but also solve the problem of

inconsistent detections by separately using three-component waveforms to compute the cross-correlation coefficients, which reduces the false detections (Yang et al., 2009).

In practice, we used 2- to 8-Hz bandpass-filtered waveforms of 85 aftershocks as template waveforms and a 3 s time window that starts at 0.5 s before the P- or S-wave arrival to perform cross-correlation with the OBS continuous waveforms. Prior to performing the cross-correction, we computed the signal-to-noise ratio, which is defined as the squared amplitude of the waveform 0.5 s after P or S arrival time divided by the squared amplitude of the waveform 0.5 s before P or S arrival time, for each template waveform. The Z-component of the velocity-type waveform was used to calculate the P-wave signal-to-noise ratio, and the N- and E-components of velocity-type waveforms were used to calculate the S-wave signal-to-noise ratios. A template is selected if the largest value between the P-and S-wave signal-to-noise ratios is greater than ten. Meanwhile, to reduce computing time, we downsampled both the template data and continuous waveform data from the original 125 Hz to 20 Hz. After visually comparing the waveforms of the template events to those of the detected events, we set the threshold value of the normalized cross-correlation coefficient to be 0.8 to identify additional events (Figs. 7a and b). We declare a candidate for an additional similar event detected for a given template event if the value of the normalized cross-correlation coefficient for at least one station is greater than 0.8. If more than one candidate is identified within a two-minute time window, the candidate with the maximum normalized cross-correlation coefficient is selected. The hypocenter location of an additional event is assigned to the location of the corresponding template event. This is incorrect for all events, but our intent is to know where more earthquakes related to aftershocks tend to occur rather than precisely locating new events. The detected additional events can be
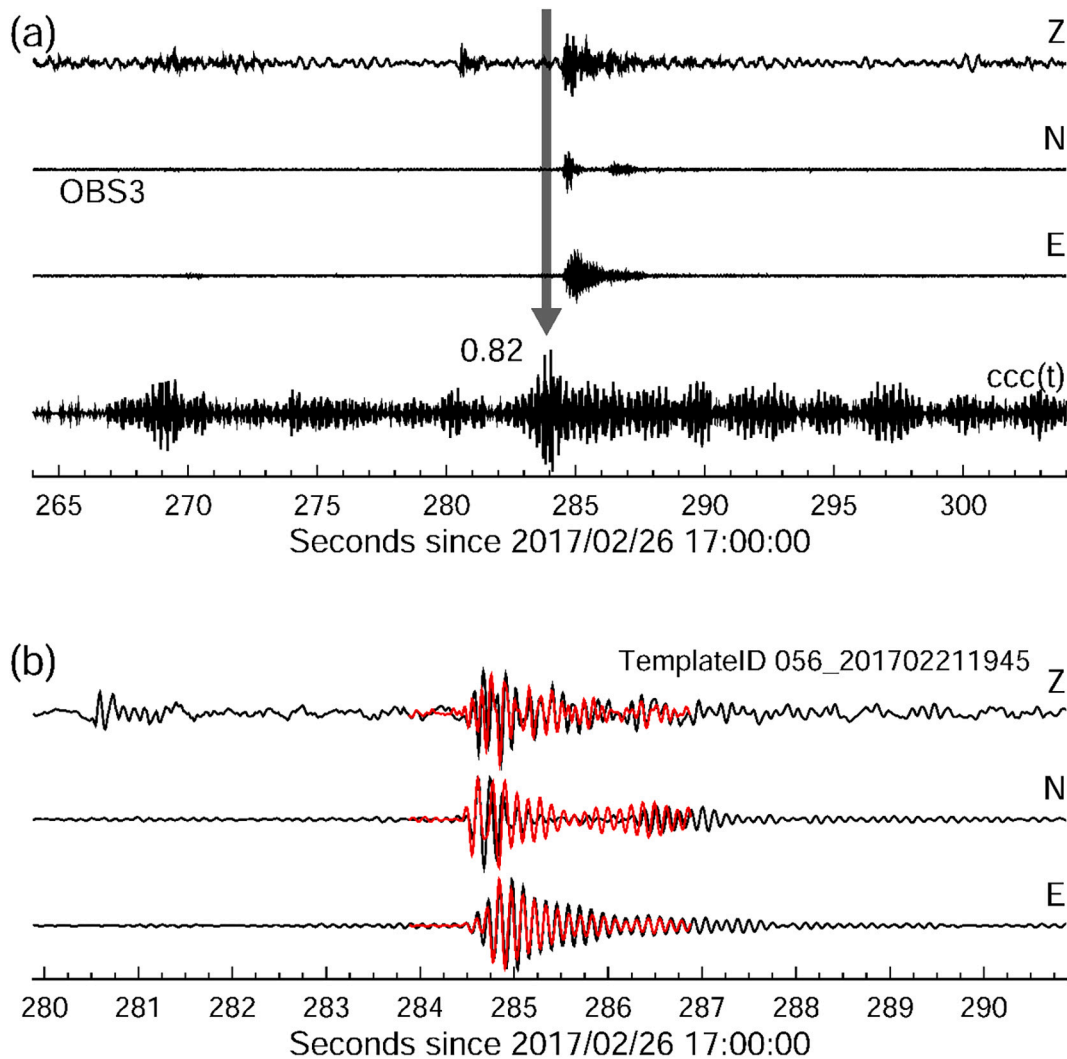
Fig. 7. (a) An example of positive detection using the sliding-window cross-correlation. The tree traces on the top are velocity-type seismograms of station OBS3. Channel names (Z, N, and E) are given on the right side. The trace at the bottom is the cross-correlation coefficient of the sliding-window cross-correlation detection using an $M_L2.1$ template event. The number marked on the trace corresponds to the maximum cross-correlation coefficient within a time window for positive detection. (b) Comparisons between the template (red) and continuous seismograms (black) in a zoom-in time window. (For interpretation of the references to colour in this figure legend, the reader is referred to the web version of this article.)

regarded as occurring at the location of the template event or its surrounding locations owing to the relatively rigorous threshold value of the normalized cross-correlation coefficient. We thus refer to these detected additional events as neighboring events in the following discussion. Additionally, because the OBSs 4 and 5 are located in the highly fractured area (Fig. 3a) and usually have relatively low signal-to-noise ratios, it is difficult to identify consistent arrivals for a neighboring event by more than three OBSs. Therefore, we did not relocate these neighboring events.

3. Results and discussion

3.1. Upper crustal low velocity structure

The inverted velocity models show that the Vp and Vs in the upper crust (<15 km) are lower than those in the Huang 1-D reference velocity model (Fig. 4c and Fig. S5). Such a low-velocity feature offshore SW Taiwan is also observed in the travel time and ambient noise tomographic images (e.g., Fan and Zhao, 2021; Huang et al., 2014; Kuo-Chen et al., 2012; Zhang et al., 2020; Zhang et al., 2018), indicating that this is an intrinsic property prevailing in the region. However, the source of

low velocity remains unclear.

Previous studies have demonstrated that Vp and Vs reduction in outer rise-trench regions is caused by the dehydration associated with bending-related faulting and fracturing of the upper elastic portion of the subducted slab at the outer rise (e.g., Fujie et al., 2013; Haberland et al., 2009; Korenaga, 2017; Ranero and Sallarès, 2004). Although our study area is not located in a typical outer rise region, the mechanism of fluid to reduce seismic velocity may also be used to explain our observations. In particular, a series of mud diapirs have been observed near the aftershock zone (Fig. 5a), and fluids and fluid-saturated mud material may exist in the subsurface (Chen et al., 2014; Doo et al., 2015a; Lin et al., 2009), reducing seismic velocity. Meanwhile, many extensional faults (Huang et al., 2004; Liu et al., 2004; Liu et al., 1997; Yang et al., 2016) and 5–10 km thick sedimentary layers (Brown et al., 2017; Deng et al., 2012; Lin et al., 2003) have been observed in the study area; hence, the fluid-filled cracks and hydrous faults may exist, decreasing seismic velocity.

In addition, our inverted 1-D velocity models are the average velocity models derived from all raypaths between the hypocenters and receivers, and as shown in Fig. 3b, a set of raypaths cover a shallower part of western Taiwan. Thus, we cannot rule out that the low-velocity

upper crust may be partially related to rays passing through the fluid-rich sediment in western Taiwan (e.g., Wu et al., 2007). The results of station delay inversion support this argument even further. As shown in Fig. S3, for most stations in western Taiwan and OBSs, the station delays are negative, indicating low velocities below the stations. At present, for our results, we cannot distinguish whether the low-velocity upper crust is dominantly caused by moisture-rich sediments, fluid-saturated mud material, dehydration of subducted plate, or a combination of these. To explore the exact source of the low-velocity structure, it is necessary to perform a high-resolution 3-D velocity inversion by deploying more OBSs off SW Taiwan.

3.2. Mid-crustal aftershocks

As a visual comparison between the relocation results by VELEST and the shrinking-box SSST method in Figs. 4, 5 and S6, the most striking feature is that most relative relocated hypocenters become shallower, that is, the average focal depth changes from the VELEST result (20.3 km) to shrinking-box SSST (12.1 km), and epicenter distributions share several common features.

Several interesting features were observed in the relocation results. First of all, the relocated aftershocks are distributed in an area with a positive free-air gravity anomaly (Figs. 5a and 6a). The gravity anomaly can be directly linked to the rock density and spatial distribution of the anomaly source rocks (e.g., Doo et al., 2020; Doo et al., 2018b; Hsu, 2001; Lebedeva-Ivanova et al., 2019; Lo et al., 2017). The presence of source rocks with a higher density than the neighboring may explain the positive free-air gravity anomaly over the study area (e.g., Doo et al., 2015b; Doo et al., 2018b; Lo et al., 2017). However, this interpretation contradicts our inverted upper crustal low-velocity and previous 3-D tomographic models (e.g., Fan and Zhao, 2021; Huang et al., 2014; Kuo-Chen et al., 2012; Zhang et al., 2020; Zhang et al., 2018) that are associated with low-density structures (Brocher, 2005). Generally, gravity anomalies result from the integrated heterogeneous density structures of the crust and upper mantle (Lebedeva-Ivanova et al., 2019). For the positive free-air gravity anomaly observed in this area, one possible explanation is that it may result from the higher density structures in the lower crust and upper mantle. Although our model did not have sufficient resolution in the upper mantle (deeper than 30 km), recent seismic tomographic models (e.g., Fan and Zhao, 2021; Zhang et al., 2020) have shown that relatively high velocity images at depths of 50–100 km. Here, our inverted low-velocity models may totally reflect the local upper crustal structure and have a minor effect on the observed gravity anomaly. An alternative interpretation is that the gravity anomaly may result from the passive margin basement arises (Doo et al., 2018a; Yeh et al., 2012). This scenario implies that the inverted low-velocity upper crust may be predominated by fluid-rich sediment in western Taiwan through seismic rays, which leads to a minor effect in generating significant gravity change.

The second observation is that most aftershocks with absolute and relative locations fall at depths of 15–25 km, and 10–15 km, respectively (Figs. 5d and 6d). Although there was a significant difference in focal depth of the absolute and relative event locations, these earthquakes may have occurred in the upper elastic portion of the subducted Eurasia lithosphere by assuming that the crustal thickness of the Eurasia lithosphere is 30 km on average (e.g., Brown et al., 2017). It is interesting that the relocated earthquakes tend to be located at middle-lower-crustal depths (10–25 km). To understand whether the predominant middle-lower-crustal earthquakes in the study area are anomalous features, we determined the frequency distribution of the focal depth in the major aftershock zone from the background seismicity with well-constrained depths of a relocated seismicity catalog from 1990 to 2016 (Wu et al., 2017; Wu et al., 2008). The relocation error of these well-constrained background seismicity (72 events) is 0.26 ± 0.26 and 0.20 ± 0.17 km in horizontal and vertical direction on average, respectively. The focal depth histogram of the background seismicity

shows that earthquakes dominantly occur in the depth range of 15–25 km, and seismic activity in the upper crust (<10 km) is less active, which agrees well with the depth distribution of the earthquake absolute location (Fig. 5d). This indicates that earthquakes tend to occur in the lower crust, which is a common seismogenic characteristic in this region.

The depth distribution pattern of the inverted aftershocks is similar to that beneath the offshore accretionary wedge of SW Taiwan; that is, earthquakes dominantly occurred in the upper mantle and seismic activity was less in the accretionary wedge (Lin et al., 2009; Wu et al., 2017). Lin et al. (2009) proposed the weak rheology of the accreted material to explain the aseismic accretionary wedge and high pore fluid pressure from the mantle to interpret the predominant mantle earthquakes. This may provide a plausible explanation for background hypocenter distribution in the study area. However, the Tainan earthquake sequence most likely results from the plate bending of the Eurasia lithosphere at the Manila Trench, which will be discussed later in Section 3.4.

Third, most aftershocks occurred to the west of the DF and formed a major NE-SW trending seismogenic zone with a length of 15 km and a width of 8 km near the surface trace of the DF, which is consistent with one of the nodal planes of the mainshock and 0212 event focal mechanism solutions (Figs. 5 and 6; Table 1). This observation implies that the DF may play a crucial role in dominating the occurrence of earthquakes. However, because of the lack of the depth resolution of DF, the spatial correlation between the Tainan earthquake sequence and the DF remains to be further studied with more complete earthquake catalog data and other geophysical observations.

Based on the aftershock distribution, the estimated fault area of 120 km² (15 km in length times 8 km in width) is approximately 2 to 11 times larger than those of 11 to 55 km², as determined by an empirical relationship between the moment magnitude (Mw5.3) and earthquake rupture area with uncertainties for a new normal fault (Wells and Coppersmith, 1994). Thus, we suggest that the rupturing related to the Tainan earthquake results from the reactivation of pre-existing faults rather than the rupture of a new fault. This explanation is also supported by the numerical experiments (e.g., Lester et al., 2012). We realize that the spatial distribution of aftershocks may be dominated by co-seismic stress release and post-seismic slip, and the aftershock zone area might not represent the true earthquake rupture area (Neo et al., 2020). However, the earthquake rupture area in the empirical relationship of Wells and Coppersmith (1994) was also determined by using the spatial distribution of early aftershocks. Hence, the earthquake rupture area estimated from the empirical relationship and ours have the same underlying variability and can be comparable to each other.

Finally, from the results of principal component analysis (Fig. 8), the value of the planarity is 0.72 ± 0.09, indicating that the aftershock distribution has a relatively high degree of planarity. The azimuth of the longest axis is $150 \pm 48°N$ with a dip angle of $27 \pm 14°$ explaining 57% of the variance (Fig. 8b), and the azimuth of the intermediate and shortest axes is $208 \pm 52°N$ and $288 \pm 131°N$ with dip angles of $24 \pm 16°$ and $48 \pm 9°$ explaining the remaining 31% and 12% of the variance (Fig. 8c), respectively. The direction of the longest axis can be well explained by the apparent NW-SE strike and SE dipping distribution of the aftershock epicenters (Fig. 8b). Moreover, regardless of the dipping angle, both the azimuths of the longest and intermediate axes, which dominantly explain 88% of the variance, are well consistent with the strike directions of the nodal planes of the mainshock and 0212 event (Fig. 8a). We also note that the bootstrap-derived error is approximately 50° for the longest and intermediate axes. If we further consider the standard error, the longest axis may change to the NE-SW direction, and the intermediate axis may change to the NW-SE direction. This highlights the importance of the NE-SW trending distribution of the event location in determining the geometric properties of the aftershock distribution. These observations demonstrate that the spatial distribution of aftershocks has significantly correlated with the focal mechanism of

Table 1

Source parameters of the events used in Fig. 10, which come from the AutoBATS moment tensor catalog (http://tecws1.earth.sinica.edu.tw/AutoBATS).

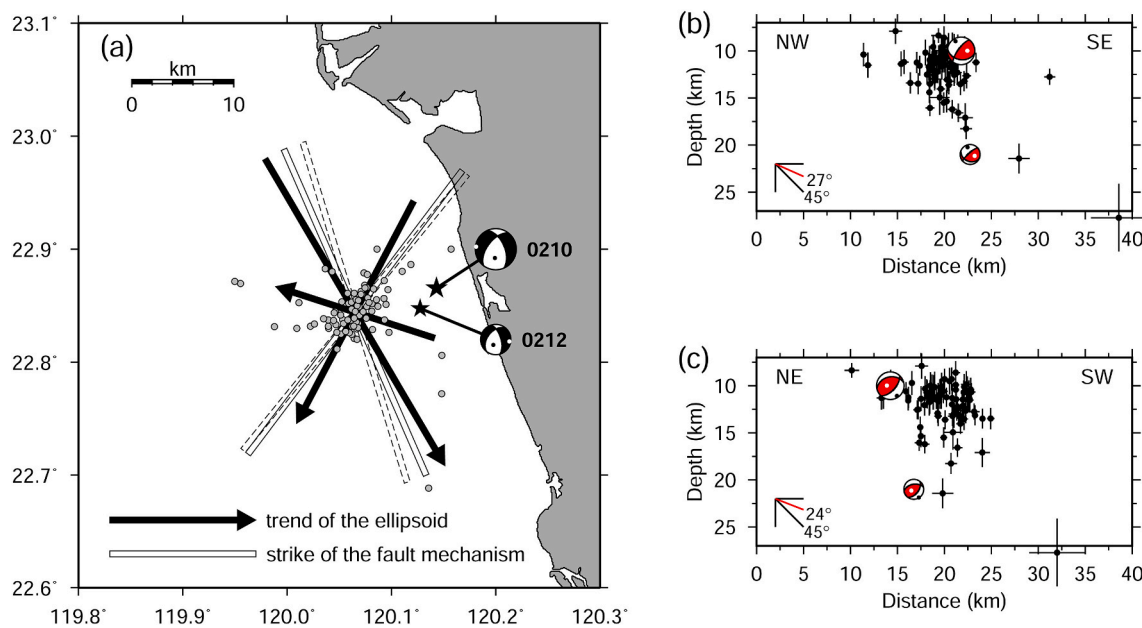| Event | Date (year/month/day/h/min/s) | Lon. (E°) | Lat. (N°) | Centroid depth (km) | Mw | Strike1 | Dip1 | Rake1 |
						Strike2	Dip2	Rake2
0210	2017/02/10/17/12/52.56	120.1431	22.8656	10	5.25	336.49	54.27	−135.92
						217.00	55.62	−45.04
0214	2017/02/12/04/30/58.81	120.1275	22.8476	21	3.82	219.04	43.74	−43.43
						343.42	61.63	−124.78
1	2009/01/10/17/26/35.79	120.2198	23.0326	9	3.26	263.72	32.80	−21.52
						12.05	78.54	−120.94
2	2015/09/16/17/16/46.93	120.0973	23.0046	13	3.73	256.99	40.76	−60.11
						33.79	55.53	−113.25
3	2016/06/29/20/50/49.71	120.0890	22.9943	16	3.32	78.33	42.91	−87.08
						254.34	47.16	−92.71
4	2018/07/11/12/41/49.50	120.2143	23.0305	9	4.02	274.32	69.48	0.36
						184.19	89.66	159.48
5	2018/08/03/16/26/30.55	120.0325	22.9856	17	3.35	189.63	43.45	−144.12
						71.93	66.23	−52.49
6	2018/08/04/11/53/27.37	120.0270	22.9943	8	3.54	228.09	41.12	−78.89
						33.48	49.81	−99.55

Fig. 8. Trends of seismicity from the principal component analysis. The longest, intermediate and shortest arrows are the longest, intermediate, and shortest axes of the ellipsoid, respectively. The solid-line and dashed-line bars represent the strikes of the focal mechanism solutions of the 0210 event (mainshock) and 0212 event (aftershock), respectively.

the mainshock and illustrates a conjugate fault system that consists of a NW-SE strike and SE-dipping fault, and an NE-SW strike and SW dipping fault.

For the neighboring event detection result (Fig. 9), the average number of detected neighboring events was 46, with a standard deviation of 69, and four aftershock templates did not detect any neighboring event. A large percentage (72%) of template events has a rather low neighboring event detection rate (< 46 events), and these events are mostly distributed in the major NE-SW trending seismogenic zone (Fig. 9a left panel), which implies that these locations may release most seismic strain energy and have insufficient time to accumulate seismic strain to occur earthquakes. The event with the maximum number of detected neighboring events (324) is located near the surface trace of the DF. Moreover, the events with a high detection rate (> 115 events) of the neighboring event are distributed on two orthogonal planes: one is NE-SW trending and SW dipping, and the other is NW-SE trending and SE dipping (Fig. 9a right panel). This further supports the existence of the conjugate fault system, as revealed by the principal component analysis.

3.3. Seismogenic mechanism

The Tainan earthquake sequence is in the northern termination of the Manila Trench, which is considered to be closely related to the transition from subduction to collision. To further constrain the seismogenic mechanism of this earthquake sequence, it is critical to know the detailed configuration of the subducted Eurasia Plate and the regional state of stress. Unfortunately, as shown in Fig. 10 in our study area, the upper plate boundary of the subducted Eurasia Plate is poorly constrained, and the exact location of the slab edge remains unclear in terms of the 3-D P-wave velocity model (Huang et al., 2014) and the relocated seismicity (Wu et al., 2008).

Here, we used the fault planes of the low-angle thrust earthquakes from the archived AutoBATS moment tensor catalog (Jian et al., 2018) from March 1996 to March 2021 to constrain the subducted interface between the Eurasia Plate and Philippine Sea Plate (e.g., Heuret et al., 2011; Kao and Chen, 1991; Kao et al., 1998; Seno, 2005). From the inferred slab geometry and the location of the Manila Trench, the
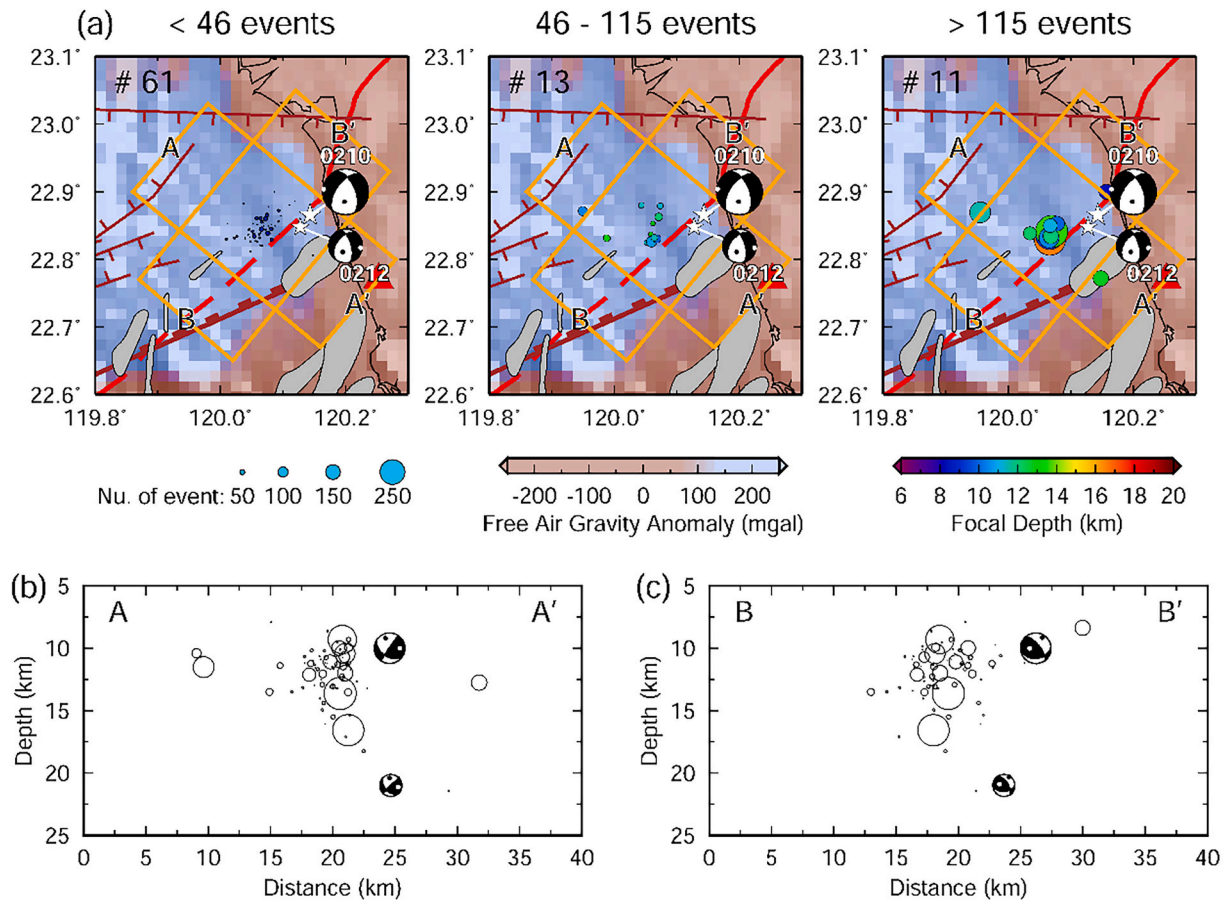
Fig. 9. Results of the detected neighboring events by using the sliding-window cross-correlation method. (a) Spatial distribution of the template events with the number of the detected neighboring events. Layout and symbols are the same as that in Fig. 5. The location of the two cross-sections is shown in (a). The A-A' cross-section oriented perpendicular to the strike of the DF is in (b), and the B-B′ cross-section oriented parallel to the strike of the DF is in (c). The size of the circles is proportional to the number of the detected neighboring events.

mainshock and aftershocks are in the outer-rise region of the subducted Eurasia Plate (Figs. 10a and b). Meanwhile, according to the normal-faulting focal mechanisms of the mainshock and 0212 event, the explanation of the occurrence of the Tainan earthquake is mostly attributed to the bending stresses of the subducted Eurasia Plate at the Manila Trench (e.g., Craig et al., 2014). This explanation is further supported by the numerical modeling results, which demonstrated that plate bending at the Manila Trench may dominate the occurrence of normal faulting off SW Taiwan (Lester et al., 2012).

In our study area, in addition to the mainshock and 0212 event, only the other six events had focal mechanism solutions in the AutoBATS moment tensor catalog (Table 1). These six events were distributed to the north of the aftershock zone, and only events 1 and 4 were located inland (Fig. 10c). At the first glance, these six events separate from the aftershock zone, and the azimuth of the P-axis of their focal mechanisms are different from those of the mainshock and 0212 events. This implies that they may not belong to the same seismogenic structure associated with the Tainan earthquake sequence. However, most focal mechanisms of these six events exhibit a normal-faulting stress regime, as shown in the depth profile (Fig. 10d), the nodal planes of events 2, 3, 5, and 6 are consistent with the rupture planes of the mainshock and 0212 event. These observations further argue that these six events may be related to the Tainan earthquake sequence, which may be mainly controlled by the bending stresses of the subducted Eurasia Plate. Additionally, events 1 and 4 occurred in almost the same location but had distinct focal mechanisms (Fig. 10c and Table 1), that is, the focal mechanism of event 1 is normal faulting, while that of event 4 is strike-slip faulting. The location of events 1 and 4 may represent an area where the slab-

bending-dominant normal-faulting focal mechanism becomes the extrusion-dominant strike-slip focal mechanism (e.g., Kao and Jian, 2001; Wu et al., 2010).

3.4. Seismic hazard issue for the slab-flexural-related earthquake

It is worth mentioning again that the Tainan earthquake sequence occurred in a place with relatively low seismic activity (Fig. 2). This is reminiscent of the twin large (M_L = 7.0) earthquakes that occurred offshore SW Taiwan on December 26, 2006 (hereinafter referred to as the Pingtung earthquake doublet), which were also located in a seismically quiescent area (Ma and Liang, 2008) (Fig. 1).

The first earthquake of the Pingtung earthquake doublet was a normal-faulting mechanism and was inferred to be caused by the bending (Kaus et al., 2009) or unbending (Liao et al., 2008) stresses of the subducted Eurasia Plate and released accumulated seismic strain to trigger the second strike-slip faulting event (Lee et al., 2008). We realize that the Pingtung earthquake doublet occurred in the incipient arc-continent collision zone, whereas the Tainan earthquake occurred in the transition zone from subduction to collision. Although the Pingtung earthquake doublet and Tainan earthquake occurred in distinct tectonic settings and have different seismogenic mechanisms, both are associated with slab bending rather than the subduction plate interface.

Recently, seismic hazard assessments of the Taiwan region have mostly relied on the identified fault geometry for consideration (e.g., Shyu et al., 2020; Wang et al., 2016; Wu et al., 2017). For seismic hazards induced by subduction earthquakes, more attention has been paid to interplate events (e.g., Heuret et al., 2011; Hsu et al., 2013; Hsu
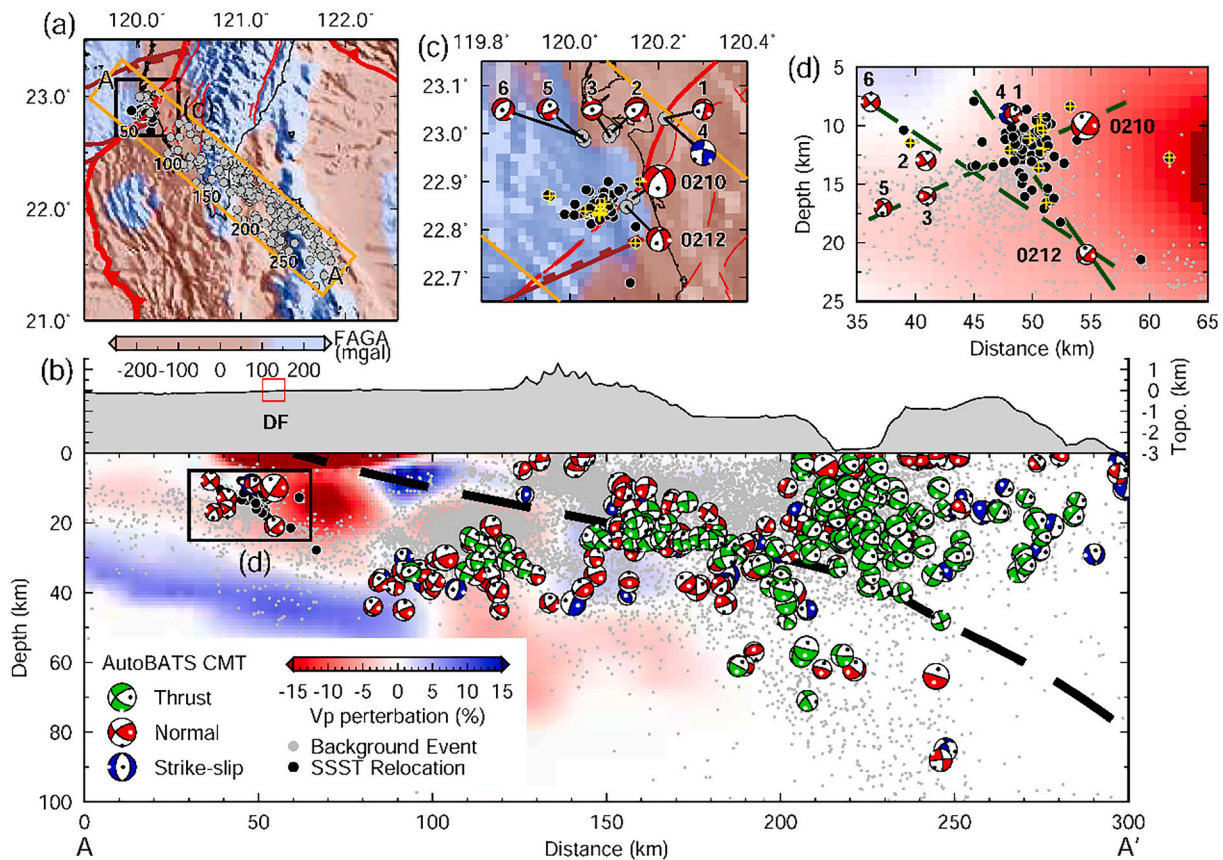
Fig. 10. (a) Spatial distribution of our relocated aftershocks (black circles) by the shirking-box SSST algorithm and the events (gray circles) from the AutoBATS moment tensor solution catalog between March 1996 and March 2021. Cross-section along the profile (A-A') is shown in (b). The square area with the black line is zoon-in in (c). Free-air gravity anomalies (FAGA) are superimposed on the bathymetry of the study area. Layout and symbols are the same as that in Fig. 5a. (b) A vertical profile A-A' showing the distribution of our relocated aftershocks (black circles), background seismicity (gray dots) from the seismicity relocation catalog of Wu et al. (2008) betwen January 1990 and December 2016, and focal mechanism solutions (in a back-hemisphere projection) from the AutoBATS moment tensor catalog. Background velocity perturbation is from Huang et al. (2014). Local bathymetry and topography are plotted at the top of the profile. The upper boundary of the subducted Eurasia Plate (thick dashed line) is inferred from low-angle thrust earthquakes. The square area outlined with red colour indicates the potential location of the deformation front (DF). (c) The zoom-in plot of source area in (a). The focal mechanism solutions from the AutoBATS catalog are plotted in a low-hemisphere projection, and the source parameters are listed in Table 1. (d) The zoom-in plot of source area in (b). Dashed lines denote the possible rupture planes in the source area. Crosses with orange colour in (c) and (d) are the aftershock locations with a high detection rate (>115 events) of the neighboring event. (For interpretation of the references to colour in this figure legend, the reader is referred to the web version of this article.)

et al., 2012; Hsu et al., 2016; Kao, 1998), whereas slab flexural-related earthquakes have been less considered. Additionally, based on the numerical modeling results, Tan (2020) suggested that in the northern portion of the Manila Trench, the plate stress was alleviated and the probability of generating a large megathrust event was relatively low, which was also identified from the weak plate coupling status by Lo et al. (2017). However, even though the numerical simulation results can truly reflect the local tectonic situation, the occurrence of medium-sized interplate or slab flexural-related events or both cannot be completely ruled out. Most importantly, previous studies have demonstrated that even if it is a medium-sized earthquake, if the rupture directivity of the event and the site effect are multiplied by each other, an intermediate-sized earthquake may cause severe disasters (Kanamori et al., 2017; Lee et al., 2016). Furthermore, the thickness of sediment offshore SW Taiwan is thick, and the effect of the thick sediment on wave propagation and amplification of ground motion in SW Taiwan remains unknown. As addressed in the Introduction section, a set of normal faults off SW Taiwan have been identified in our study area, and the possibility of reactivation of preexisting normal faults (such as the Tainan earthquake) to generate landslides or tsunamis or both cannot be completely ruled out (Chin et al., 2019). Therefore, we suggest that slab flexural-related earthquakes in the subduction zone, particularly off SW Taiwan, should be considered in seismic hazard analysis in addition to

interplate events.

4. Conclusions

We used the joint travel time data of the OBSs and CWB inland stations to simultaneously determine the 1-D Vp and Vs velocity models and aftershock hypocenters of the Tainan earthquake. With the deployment of OBSs, the station coverage is largely improved; the inverted velocity models and aftershock locations are thus more reliable. Our inverted velocity models show a low-velocity upper crust, which seems to be an intrinsic feature in and off SW Taiwan. The relative relocated aftershocks were mostly confined at 10–15 km depth, while most of the absolute relocated aftershocks were located at 15–25 km depth, which is consistent with the focal depth pattern of background seismicity. The relocated epicenters were in an area with a positive free-air gravity anomaly and were not linked to any known active faults inland. Most epicenters were located to the west of the surface trace of the DF and were closely aligned subparallel to the DF. The DF seems to be a barrier to inhibiting earthquake ruptures, but this calls for additional examinations with more data. A conjugate fault system composed of a SW-dipping NE-SW trending fault and a SE-dipping NW-SE tending fault can explain the geometrical properties of the aftershock distribution. We demonstrated, using focal mechanism solutions and aftershock

distribution, that the Tainan earthquake is a reactivated outer-rise event caused by bending stresses of the subducted Eurasia Plate at the Manila Trench. In contrast to interplate earthquakes, the outer-rise events have received little attention in seismic hazard assessments in Taiwan. As two subduction zones around the Taiwan region, earthquakes related to the bending stresses of the subducted plate are expected. In particular, the normal faulting results from the plate bending may cause tsunamis or landslide tsunamis or both. Therefore, the seismic hazard for the flexural-related events in Taiwan requires more attention for seismic and tsunami hazard analyses.

Declaration of Competing Interest

The authors declare that they have no known competing financial interests or personal relationships that could have appeared to influence the work reported in this paper.

Acknowledgments

Appendix A. Supplementary data

Supplementary data to this article can be found online at https://doi.org/10.1016/j.tecto.2021.228995.

References

Aochi, H., Fukuyama, E., Matsu'ura, M., 2000. Spontaneous rupture propagation on a non-planar fault in 3-D elastic medium. Pure Appl. Geophys. 157, 2003–2027.
Auffret, Y.P., Klingelhoefer, F.J.C., Lin, J.-Y., Sibuet, J.-C., 2004. MicrOBS: a new ocean bottom seismometer generation. First Break 22, 41–47.
Bai, K., Ampuero, J.-P., 2017. Effect of seismogenic depth and background stress on physical limits of earthquake rupture across fault step overs. J. Geophys. Res. Solid Earth 122, 10280–210298.
Brocher, T.M., 2005. Empirical relations between elastic wavespeeds and density in the Earth's crust. Bull. Seism. Soc. Am. 95, 2081–2092.
Brown, D., Alvarez-Marron, J., Biete, C., Kuo-Chen, H., Camanni, G., Ho, C.-W., 2017. How the structural architecture of the Eurasian continental margin affects the structure, seismicity, and topography of the south central Taiwan fold-and-thrust belt. Tectonics 36, 1275–1294.
Chen, Y.-L., Shin, T.-C., 1998. Study on the earthquake location of 3-D velocity structure in the Taiwan area. Meteor. Bull. 42, 135–169.
Chen, S.-C., Hsu, S.-K., Wang, Y., Chung, S.-H., Chen, P.-C., Tsai, C.-H., Liu, C.-S., Lin, H.-S., Lee, Y.-W., 2014. Distribution and characters of the mud diapirs and mud volcanoes off southwest Taiwan. J. Asian Earth Sci. 92, 201–214.
Chin, S.-J., Lin, J.-Y., Yeh, Y.-C., Kuo-Chen, H., Liang, C.-W., 2019. Seismotectonic characteristics of the Taiwan collision-Manila subduction transition: the effect of pre-existing structures. J. Asian Earth Sci. 173, 113–120.
Craig, T.J., Copley, A., Jackson, J., 2014. A reassessment of outer-rise seismicity and its implications for the mechanics of oceanic lithosphere. Geophys. J. Int. 197, 63–89.

Deng, J.-M., Wang, T.K., Yang, B.J., Lee, C.-S., Liu, C.-S., Chen, S.-C., 2012. Crustal velocity structure off SW Taiwan in the northernmost South China Sea imaged from TAIGER OBS and MCS data. Mar. Geophys. Res. 33, 327–349.
Diehl, T., Kissling, E., Husen, S., Aldersons, F., 2009. Consistent phase picking for regional tomography models: application to the greater Alpine region. Geophys. J. Int. 176, 542–554.
Doo, W.-B., Hsu, S.-K., Lo, C.-L., Chen, S.-C., Tsai, C.-H., Lin, J.-Y., Huang, Y.-P., Huang, Y.-S., Chiu, S.-D., Ma, Y.-F., 2015a. Gravity anomalies of the active mud diapirs off southwest Taiwan. Geophys. J. Int. 203, 2089–2098.
Doo, W.-B., Lo, C.-L., Kuo-Chen, H., Brown, D., Hsu, S.-K., 2015b. Exhumation of serpentinized peridotite in the northern Manila subduction zone inferred from forward gravity modeling. Geophys. Res. Lett. 42, 7977–7982.
Doo, W.-B., Lo, C.-L., Hsu, S.-K., Tsai, C.-H., Huang, Y.-S., Wang, H.-F., Chiu, S.-D., Ma, Y.-F., Liang, C.-W., 2018a. New gravity anomaly map of Taiwan and its surrounding regions with some tectonic interpretations. J. Asian Earth Sci. 154, 93–100.
Doo, W.-B., Lo, C.-L., Wu, W.-N., Lin, J.-Y., Hsu, S.-K., Huang, Y.-S., Wang, H.-F., 2018b. Strength of plate coupling in the southern Ryukyu subduction zone. Tectonophysics 723, 223–228.
Doo, W.-B., Lo, C.-L., Kuo-Chen, H., Huang, Y.-S., Wu, W.-N., Hsu, S.-K., Wang, H.-F., 2020. Variations in mantle lithosphere buoyancy reveal seismogenic behaviour in the Sunda–Andaman subduction zone. Geophys. J. Int. 220, 1275–1283.
Dziewonski, A.M., Chou, T.-A., Woodhouse, J.H., 1981. Determination of earthquake source parameters from waveform data for studies of global and regional seismicity. Phys. Earth Planet. Interi. 86, 2825–2852.
Fan, J., Zhao, D., 2021. P-wave tomography and azimuthal anisotropy of the Manila-Taiwan-Southern Ryukyu Region. Tectonics 40 e2020TC006262.
Fujie, G., Kodaira, S., Yamashita, M., Sato, T., Takahashi, T., Takahashi, N., 2013. Systematic changes in the incoming plate structure at the Kuril trench. Geophys. Res. Lett. 40, 88–93.
Gibbons, S.J., Ringdal, F., 2006. The detection of low magnitude seismic events using array-based waveform correlation. Geophys. J. Int. 165, 149–166.
Haberland, C., Rietbrock, A., Lange, D., Bataille, K., Dahm, T., 2009. Structure of the seismogenic zone of the southcentral Chilean margin revealed by local earthquake traveltime tomography. J. Geophys. Res. Solid Earth 114.
Han, W.-C., Liu, C.-S., Chi, W.-C., Chen, L., Lin, C.-C., Chen, S.-C., 2017. Westward advance of the deformation front and evolution of submarine canyons offshore of southwestern Taiwan. J. Asian Earth Sci. 149, 6–19.
Heuret, A., Lallemand, S., Funiciello, F., Piromallo, C., Faccenna, C., 2011. Physical characteristics of subduction interface type seismogenic zones revisited. Geochem. Geophys. Geosyst. 12, Q01004.
Hicks, S.P., Rietbrock, A., Ryder, I.M.A., Lee, C.-S., Miller, M., 2014. Anatomy of a megathrust: the 2010 M8.8 Maule, Chile earthquake rupture zone imaged using seismic tomography. Earth Planet. Sci. Lett. 405, 142–155.
Hsu, S.-K., 2001. Lithospheric structure, buoyancy and coupling across the southernmost Ryukyu subduction zone: an example of decreasing plate coupling. Earth Planet. Sci. Lett. 186, 471–478.
Hsu, Y.-J., Ando, M., Yu, S.-B., Simons, M., 2012. The potential for a great earthquake along the southernmost Ryukyu subduction zone. Geophys. Res. Lett. 39, L14302.
Hsu, S.-K., Yeh, Y.-C., Sibuet, J.-C., Doo, W.-B., Tsai, C.-H., 2013. A mega-splay fault system and tsunami hazard in the southern Ryukyu subduction zone. Earth Planet. Sci. Lett. 362, 99–107.
Hsu, Y.-J., Yu, S.-B., Loveless, J.P., Bacolcol, T., Solidum, R., Luis Jr., A., Pelicano, A., Woessner, J., 2016. Interseismic deformation and moment deficit along the Manila subduction zone and the Philippine Fault system. J. Geophys. Res. Solid Earth 121, 7639–7665.
Huang, S.-T., Yang, K.-M., Hung, J.-H., Wu, J.-C., Ting, H.-H., Mei, W.-W., Hsu, S.-H., Lee, M., 2004. Deformation front development at the northeast margin of the Tainan Basin, Tainan–Kaohsiung Area, Taiwan. Mar. Geophys. Res. 25, 139–156.
Huang, H.-H., Wu, Y.-M., Song, X., Chang, C.-H., Lee, S.-J., Chang, T.-M., Hsieh, H.-H., 2014. Joint Vp and Vs tomography of Taiwan: implications for subduction-collision orogeny. Earth Planet. Sci. Lett. 392, 177–191.
Jian, P.R., Tseng, T.L., Liang, W.T., Huang, P.H., 2018. A new automatic full-waveform regional moment tensor inversion algorithm and its applications in the Taiwan Area. Bull. Seism. Soc. Am. 108, 573–587.
Kanamori, H., Ye, L., Huang, B.-S., Huang, H.-H., Lee, S.-J., Liang, W.-T., Lin, Y.-Y., Ma, K.-F., Wu, Y.-M., Yeh, T.-Y., 2017. A strong-motion hot spot of the 2016 Meinong, Taiwan, earthquake (Mw = 6.4). Terr. Atmos. Ocean. Sci. 28, 637–650.
Kao, H., 1998. Can great earthquakes occur in the southernmost Ryukyu Arc - Taiwan region? Terr. Atmos. Oceanic Sci. 9, 487–508.
Kao, H., Chen, W.-P., 1991. Earthquakes along the Ryukyu-Kyushu arc: Strain segmentation, lateral compression, and the thermomechanical state of the plate interface. J. Geophys. Res. Solid Earth 96, 21,443–421,485.
Kao, H., Chen, W.-P., 2000. The Chi-Chi earthquake sequence: active, out-of-sequence thrust faulting in Taiwan. Science 288, 2346–2349.
Kao, H., Jian, P.-R., 2001. Seismogenic patterns in the Taiwan region: insights from source parameter inversion of BATS data. Tectonophysics 333, 179–198.
Kao, H., Shen, S.-S.J., Ma, K.-F., 1998. Transition from oblique subduction to collision: Earthquakes in the southernmost Ryukyu arc-Taiwan region. J. Geophy. Res. Solid Earth 103, 7211–7229.
Kaus, B.J.P., Liu, Y., Becker, T.W., Yuen, D.A., Shi, Y., 2009. Lithospheric stress-states predicted from long-term tectonic models: Influence of rheology and possible application to Taiwan. J. Asian Earth Sci. 36, 119–134.
Kissling, E., Ellsworth, W.L., Eberhart-Phillips, D., Kradolfer, U., 1994. Initial reference models in local earthquake tomography. J. Geophys. Res. Solid Earth 99, 19635–19646.

Korenaga, J., 2017. On the extent of mantle hydration caused by plate bending. Earth Planet. Sci. Lett. 457, 1–9.

Kuo-Chen, H., Wu, F.T., Roecker, S.W., 2012. Three-dimensional P velocity structures of the lithosphere beneath Taiwan from the analysis of TAIGER and related seismic data sets. J. Geophys. Res. Solid Earth 117, B06306.

Lange, D., Tilmann, F., Barrientos, S.E., Contreras-Reyes, E., Methe, P., Moreno, M., Heit, B., Agurto, H., Bernard, P., Vilotte, J.-P., Beck, S., 2012. Aftershock seismicity of the 27 February 2010 Mw 8.8 Maule earthquake rupture zone. Earth Planet. Sci. Lett. 317-318, 413–425.

Lebedeva-Ivanova, N., Gaina, C., Minakov, A., Kashubin, S., 2019. ArcCRUST: arctic crustal thickness from 3-D gravity inversion. Geochem. Geophys. Geosyst. 20, 3225–3247.

Lee, S.-J., Liang, W.-T., Huang, B.-S., 2008. Source mechanisms and rupture processes of the 26 december 2006 pingtung earthquake doublet as determined from the regional seismic records. Terr. Atmos. Ocean. Sci. 19, 555–565.

Lee, S.J., Yeh, T.Y., Lin, Y.Y., 2016. Anomalously large ground motion in the 2016 ML 6.6 Meinong, Taiwan, earthquake: a synergy effect of source rupture and site amplification. Seismol. Res. Lett. 87, 1319–1326.

Lester, R., Lavier, L.L., McIntosh, K., Avendonk, H.J.A.V., Wu, F.T., 2012. Active extension in Taiwan's precollision zone: a new model of plate bending in continental crust. Geology 40, 831–834.

Lester, R., Van Avendonk, H.J.A., McIntosh, K., Lavier, L., Liu, C.S., Wang, T.K., Wu, F., 2014. Rifting and magmatism in the northeastern South China Sea from wide-angle tomography and seismic reflection imaging. J. Geophys. Res. Solid Earth 119, 2305–2323.

Liao, Y.-C., Hsu, S.-K., Chang, C.-H., Doo, W.-B., Ho, M.-Y., Lo, C.-L., Lee, C.-S., 2008. Seismic tomography off SW Taiwan: a joint inversion from OBS and onshore data of 2006 Pingtung aftershocks. Terr. Atmos. Ocean. Sci. 19, 729–741.

Liao, W.-Z., Lin, A.T., Liu, C.-S., Oung, J.-N., Wang, Y., 2016. A study on tectonic and sedimentary development in the rifted northern continental margin of the South China Sea near Taiwan. Interpretation 4, SP47–SP65.

Lin, Y.-W., 2013. Structure of the Subduction Zone South of Taiwan Constrained by OBS Data, Department of Geosciences. National Taiwan University, p. 104.

Lin, G., 2018. The source-specific station term and waveform cross-correlation earthquake location package and its applications to California and New Zealand. Seismol. Res. Lett. 89, 1877–1885.

Lin, G., Okubo, P.G., 2020. Seismic evidence for a shallow detachment beneath Kīlauea's south flank during the 2018 activity. Geophys. Res. Lett. 47 e2020GL088003.

Lin, G., Shearer, P., 2005. Tests of relative earthquake location techniques using synthetic data. J. Geophys. Res. Solid Earth 110, B04304.

Lin, A.T., Watts, A.B., Hesselbo, S.P., 2003. Cenozoic stratigraphy and subsidence history of the South China Sea margin in the Taiwan region. Basin Res. 15, 453–478.

Lin, A.T., Liu, C.-S., Lin, C.-C., Schnurle, P., Chen, G.-Y., Liao, W.-Z., Teng, L.S., Chuang, H.-J., Wu, M.-S., 2008. Tectonic features associated with the overriding of an accretionary wedge on top of a rifted continental margin: an example from Taiwan. Mar. Geol. 255, 186–203.

Lin, A.T.-S., Yao, B., Hsu, S.-K., Liu, C.-S., Huang, C.-Y., 2009. Tectonic features of the incipient arc-continent collision zone of Taiwan: implications for seismicity. Tectonophysics 479, 28–42.

Liu, C.-S., Huang, I.L., Teng, L.S., 1997. Structural features off southwestern Taiwan. Mar. Geol. 137, 305–319.

Liu, C.-S., Deffontaines, B., Lu, C.-Y., Lallemand, S., 2004. Deformation patterns of an accretionary wedge in the transition zone from subduction to collision offshore southwestern Taiwan. Mar. Geophys. Res. 25, 123–137.

Lo, C.-L., Doo, W.-B., Kuo-Chen, H., Hsu, S.-K., 2017. Plate coupling across the northern Manila subduction zone deduced from mantle lithosphere buoyancy. Phys. Earth Planet. Inter. 273, 50–54.

Ma, K.-F., Liang, W.-T., 2008. Preface to the 2006 Pingtung earthquake doublet special issue. Terr. Atmos. Oceanic Sci. 19, I–III.

Michelini, A., Bolt, B.A., 1986. Application of the principal parameters method to the 1983 Coalinga, California, aftershock sequence. Bull. Seism. Soc. Am. 76, 409–420.

Neo, J.C., Huang, Y., Yao, D., Wei, S., 2020. Is the aftershock zone area a good proxy for the mainshock rupture area? Bull. Seism. Soc. Am. 111, 424–438.

Pang, G., Koper, K.D., Stickney, M.C., Pechmann, J.C., Burlacu, R., Pankow, K.L., Payne, S., Benz, H.M., 2018. Seismicity in the Challis, Idaho, region, January 2014–May 2017: late aftershocks of the 1983 Ms 7.3 Borah Peak earthquake. Seismol. Res. Lett. 89, 1366–1378.

Peng, Z., Zhao, P., 2009. Migration of early aftershocks following the 2004 Parkfield earthquake. Nat. Geosci. 2, 877–881.

Ranero, C.R., Sallarès, V., 2004. Geophysical evidence for hydration of the crust and mantle of the Nazca plate during bending at the north Chile trench. Geology 32, 549–552.

Rezaeifar, M., Kissling, E., 2018. Compilation of a high-quality catalogue for M3.0+ seismicity in northern Iran region for the period of 2005–2017. Geophys. J. Int. 215, 118–132.

Roth, M.P., Verdecchia, A., Harrington, R.M., Liu, Y., 2020. High-resolution imaging of hydraulic-fracturing-induced earthquake clusters in the Dawson-Septimus area, northeast British Columbia, Canada. Seismol. Res. Lett. 91, 2744–2756.

Sandwell, D.T., Smith, W.H.F., 1997. Marine gravity anomaly from Geosat and ERS 1 satellite altimetry. J. Geophys. Res. Solid Earth 102, 10039–10054.

Sandwell, D.T., Müller, R.D., Smith, W.H.F., Garcia, E., Francis, R., 2014. New global marine gravity model from CryoSat-2 and Jason-1 reveals buried tectonic structure. Science 346, 65–67.

Seno, T., 2005. Variation of downdip limit of the seismogenic zone near the Japanese islands: implications for the serpentinization mechanism of the forearc mantle wedge. Earth Planet. Sci. Lett. 231, 249–262.

Shearer, P.M., Hardebeck, J.L., Astiz, L., Richards-Dinger, K.B., 2003. Analysis of similar event clusters in aftershocks of the 1994 Northridge, California, earthquake. J. Geophys. Res. Solid Earth 108.

Shelly, D.R., 2020. A high-resolution seismic catalog for the initial 2019 Ridgecrest earthquake sequence: Foreshocks, aftershocks, and faulting complexity. Seismol. Res. Lett. 91, 1971–1978.

Shelly, D.R., Beroza, G.C., Ide, S., 2007. Non-volcanic tremor and low-frequency earthquake swarms. Nature 446, 305–307.

Shyu, J.B.H., Sieh, K., Chen, Y.-G., Liu, C.-S., 2005. The neotectonic architecture of Taiwan and its implications for future large earthquakes. J. Geophys. Res. Solid Earth 110, B08402.

Shyu, J.B.H., Yin, Y.-H., Chen, C.-H., Chuang, Y.-R., Liu, S.-C., 2020. Updates to the on-land seismogenic structure source database by the Taiwan Earthquake Model (TEM) project for seismic hazard analysis of Taiwan. Terr. Atmos. Ocean. Sci. 31, 469–478.

Storchak, D.A., Di Giacomo, D., Bondár, I., Harris, J., Engdahl, E.R., Lee, W.H.K., Villaseñor, A., Bormann, P., 2013. Public release of the ISC–GEM global instrumental earthquake catalogue (1900–2009). Seismol. Res. Lett. 84, 810–815.

Tan, E., 2020. Subduction of transitional crust at the Manila Trench and its geophysical implications. J. Asian Earth Sci. 187, 104100.

Tsai, M.-C., Yu, S.-B., Shin, T.-C., Kuo, K.-W., Leu, P.-L., Chang, C.-H., Ho, M.-Y., 2015. Velocity field derived from Taiwan continuous GPS array (2007-2013). Terr. Atmos. Ocean. Sci. 26, 527–556.

Wang, J.-H., 1998. Studies of earthquake seismology in Taiwan during the 1897-1996 period. J. Geol. Soc. China 41, 291–336.

Wang, Y.J., Lee, Y.T., Chan, C.H., Ma, K.F., 2016. An investigation of the reliability of the Taiwan earthquake model PSHA2015. Seismol. Res. Lett. 87, 1287–1298.

Wang, S.-Y., Hsu, S.-K., Yeh, Y.-C., 2019. Earthquake-related structures beneath the southernmost portion of the Ryukyu Arc and forearc. Geophys. Res. Lett. 46, 3717–3725.

Wells, D.L., Coppersmith, K.J., 1994. New empirical relationships among magnitude, rupture length, rupture width, rupture area, and surface displacement. Bull. Seism. Soc. Am. 84, 974–1002.

Wessel, P., Smith, W.M.F., 1998. New improved version of generic mapping tools released. EOS Trans. AGU 79, 579.

Wu, Y.-M., Chang, C.-H., Zhao, L., Shyu, J.B.H., Chen, Y.-G., Sieh, K., Avouac, J.P., 2007. Seismic tomography of Taiwan: improved constraints from a dense network of strong-motion stations. J. Geophys. Res. Solid Earth 112, B08312.

Wu, Y.-M., Chang, C.-H., Zhao, L., Teng, T.-L., Nakamura, M., 2008. A comprehensive relocation of earthquakes in Taiwan from 1991 to 2005. Bull. Seism. Soc. Am. 98, 1471–1481.

Wu, W.-N., Kao, H., Hsu, S.-K., Lo, C.-L., Chen, H.-W., 2010. Spatial variation of the crustal stress field along the Ryukyu-Taiwan-Luzon convergent boundary. J. Geophys. Res. Solid Earth 115, B11401.

Wu, W.-N., Yen, Y.-T., Hsu, Y.-J., Wu, Y.-M., Lin, J.-Y., Hsu, S.-K., 2017. Spatial variation of seismogenic depths of crustal earthquakes in the Taiwan region: implications for seismic hazard assessment. Tectonophysics 708, 81–95.

Yang, H., Zhu, L., Chu, R., 2009. Fault-plane determination of the 18 April 2008 Mount Carmel, Illinois, earthquake by detecting and relocating aftershocks. Bull. Seism. Soc. Am. 99, 3413–3420.

Yang, K.-M., Rau, R.-J., Chang, H.-Y., Hsieh, C.-Y., Ting, H.-H., Huang, S.-T., Wu, J.-C., Tang, Y.-J., 2016. The role of basement-involved normal faults in the recent tectonics of western Taiwan. Geol. Mag. 153, 1166–1191.

Yeh, Y.-C., Hsu, S.-K., Doo, W.-B., Sibuet, J.-C., Liu, C.-S., Lee, C.-S., 2012. Crustal features of the northeastern South China Sea: insights from seismic and magnetic interpretations. Mar. Geophys. Res. 33, 307–326.

Yu, H.-S., 2004. Nature and distribution of the deformation front in the Luzon Arc-Chinese continental margin collision zone at Taiwan. Mar. Geophys. Res. 25, 109–122.

Yu, S.-B., Chen, H.-Y., Kuo, L.-C., 1997. Velocity field of GPS stations in the Taiwan area. Tectonophysics 274, 41–59.

Zhang, Y., Yao, H., Yang, H.-Y., Cai, H.-T., Fang, H., Xu, J., Jin, X., Kuo-Chen, H., Liang, W.-T., Chen, K.-X., 2018. 3-D crustal shear-wave velocity structure of the Taiwan Strait and Fujian, SE China, revealed by ambient noise tomography. J. Geophys. Res. Solid Earth 123, 8016–8031.

Zhang, Y., Yao, H., Xu, M., Liu, B., 2020. Upper mantle shear wave velocity structure of southeastern China: seismic evidence for magma activities in the late Mesozoic to the Cenozoic. Geochem. Geophys. Geosyst. 21 e2020GC009103.